

1 **Probing deformation mechanisms of a FeCoCrNi high-entropy alloy at 293 and**  
2 **77 K using *in situ* neutron diffraction**

3 Yiqiang Wang<sup>a, b</sup>, Bin Liu<sup>c</sup>, Kun Yan<sup>d</sup>, Minshi Wang<sup>e</sup>, Saurabh Kabra<sup>f</sup>, Yu-Lung  
4 Chiu<sup>e</sup>, David Dye<sup>g</sup>, Peter D. Lee<sup>a, f</sup>, Yong Liu<sup>c\*\*</sup>, Biao Cai<sup>e, b\*</sup>,

5 <sup>a</sup> *Culham Centre for Fusion Energy, Culham Science Centre, Abingdon, OX13 3DB,*  
6 *UK*

7 <sup>b</sup> *Research Complex at Harwell, RAL, Harwell, Oxfordshire, OX11 0FA, UK*

8 <sup>c</sup> *The State Key Laboratory of Powder Metallurgy, Central South University, Changsha,*  
9 *410083, P.R. China*

10 <sup>d</sup> *School of Materials, University of Manchester, M13 9PL, UK*

11 <sup>e</sup> *School of Metallurgy and Materials, University of Birmingham, Birmingham*

12 <sup>f</sup> *ISIS Facility, Rutherford Appleton Laboratory, Didcot OX11 0QX, UK*

13 <sup>g</sup> *Department of Materials, Imperial College London, Exhibition Road, London SW7*  
14 *2AZ, United Kingdom*

15 **Abstract**

16 The deformation responses at 77 and 293 K of a FeCoNiCr high-entropy alloy,  
17 produced by a powder metallurgy route, are investigated using *in situ* neutron  
18 diffraction and correlative transmission electron microscopy. The strength and ductility  
19 of the alloy are significant improved at cryogenic temperatures. The true ultimate  
20 tensile strength and total elongation increased from 980 MPa and 45% at 293 K to 1725  
21 MPa and 55% at 77K, respectively. The evolutions of lattice strain, stacking fault  
22 probability, and dislocation density were determined via quantifying the *in situ* neutron  
23 diffraction measurements. The results demonstrate that the alloy has a much higher  
24 tendency to form stacking faults and mechanical twins as the deformation temperature  
25 drops, which is due to the decrease of stacking fault energy (estimated to be 32.5 mJ/m<sup>2</sup>  
26 and 13 mJ/m<sup>2</sup> at 293 and 77 K, respectively). The increased volume fraction of nano-  
27 twins and twin-twin intersections, formed during cryogenic temperature deformation,  
28 has been confirmed by transmission electron microscopy analysis. The enhanced  
29 strength and ductility at cryogenic temperatures can be attributed to the increased  
30 density of dislocations and nano-twins. The findings provide a fundamental  
31 understanding of underlying governing mechanistic mechanisms for the twinning  
32 induced plasticity in high entropy alloys, paving the way for the development of new  
33 alloys with superb resistance to cryogenic environments.

34 **Keywords:** high entropy alloy, deformation twinning, neutron diffraction, cryogenic  
35 deformation, stacking fault energy

36

## 37 **1. Introduction**

38 High-entropy alloys (HEAs) were first introduced in 2004 [1, 2], which aimed to  
39 maximise the configuration entropy to form a single phase microstructure via  
40 combining four or more principle elements in equimolar or near equimolar ratios. The  
41 high configuration entropy, sluggish diffusion, cocktail effect and large lattice  
42 distortion lead to their promising properties such as high strength, excellent ductility,  
43 and superior fracture toughness [3-8].

44 One type of HEA and its variants, based on five 3d transition elements (Fe, Co, Cr, Mn,  
45 Ni), can form a single phase face-centered-cubic (fcc) structure, displaying an excellent  
46 combination of high strength, ductility and fracture toughness at both room and  
47 cryogenic temperatures. Their mechanical properties improve significantly with  
48 decreasing deformation temperatures [3-7]. We termed this group of HEA as tHEA to  
49 distinguish them from other high entropy alloys (such as multi-phase HEAs [8]). tHEAs  
50 have attracted significant interests for cryogenic applications, such as liquid nitrogen  
51 storage and transportation of liquid gas from offshore.

52 Many microstructural studies [3-7], on strained or failed tensile specimens, have been  
53 carried out, confirming the occurrence of nano-twinning during low temperature  
54 deformation of tHEAs. Hence twinning induced plasticity is attributed to the tHEAs'  
55 superb mechanical performance. Twinning induced plasticity has been at the forefront  
56 of research recently as it is one of the micro-mechanistic mechanisms that can overcome  
57 the strength-ductility trade-off, which has been demonstrated by fcc metals and alloys  
58 with low stacking fault energy (SFE) such as the tHEAs and TWIP steels [9-11].

59 The deformation mechanisms of fcc metals and alloys are strongly related to the  
60 temperature- and composition- dependent stacking fault energy (SFE) [12]. With the  
61 drop of SFE, the deformation mechanisms change from dislocation glide alone, to  
62 dislocation glide and mechanical twinning, to dislocation glide and martensite  
63 transformation [13-15]. This has been demonstrated in many fcc metals and alloys,  
64 including austenite steels [16], TRIP and TWIP steels [3,4], and Cu-Al alloys [17]. The  
65 SFE of the tHEAs has been measured or calculated to be 10-40 mJ/m<sup>2</sup> at room  
66 temperature [18-20]. In this SFE range, deformation twinning is usually activated,  
67 which has been confirmed in tHEAs by a few experimental studies [3-7]. Recently,  
68 martensite phase transformation have been observed when tHEAs were deformed under  
69 hydrostatic high-pressure conditions [21, 22] at both room and high temperatures,  
70 demonstrating that the fcc tHEAs can be destabilized into hcp phase at high pressure  
71 (e.g. over 14 GPa [21]).

72 It is known that the SFE will drop as the temperature decreases, hence at cryogenic  
73 temperatures, the formation of shear bands, deformation twins and stacking faults can  
74 be enhanced [6, 23]. Simulations using first-principles methods [24, 25] confirm the  
75 temperature dependent behaviour of SFE and some predict that the SFE of tHEAs can  
76 even be negative at cryogenic temperatures [19, 26-28]. To validate the simulated  
77 results, the SFE of tHEAs at cryogenic temperatures need to be determined  
78 experimentally. Although a few studies have measured room temperature SFE of  
79 tHEAs using TEM based methods [18], it is not a straight-forward task to measure low

80 temperature SFE using TEM, as the samples deformed at cryogenic temperatures need  
81 to be warmed up to room temperature for sample preparation, during which the  
82 dislocation and fault structure may have changed. Thereby the development of new  
83 methods to measure low temperature SFE is critically needed, which will provide  
84 much-needed validation for the simulations[19, 26] and pave the way for designing new  
85 tHEAs.

86 To study deformation mechanisms of tHEAs, quantitative *in situ* mapping of  
87 microstructure evolution of tHEAs at room temperature has previously been carried out,  
88 using TEM [26, 29, 30], SEM [31], synchrotron X-ray diffraction [32] and neutron  
89 diffraction [33, 34]. The *in situ* TEM directly observed the motion of Shockley partials,  
90 the formation of stacking faults and 3D network of nano-twins [29, 30]. *In situ* neutron  
91 and X-ray diffraction, on the other hand, can quantify the grain-level behaviour during  
92 deformation, which includes the measurement of stacking fault probability [33], single-  
93 crystal elastic constants [34], phase transformation [32], and SFE [33]. Those *in situ*  
94 works significantly improved our understanding of the microstructural and mechanistic  
95 origin of tHEAs' superb mechanical properties. Carrying out *in situ* studies at cryogenic  
96 temperatures can provide similar benefits, not only unravelling the underlying  
97 mechanisms determining the dramatic increase of strength and ductility at cryogenic  
98 temperatures of the alloys, but also determining critical material parameters such as  
99 SFE.

100 In the current study, we conducted uniaxial tensile deformation on a FeCoCrNi high-  
101 entropy alloy at 293 and 77 K. With the help of *in situ* neutron diffraction, we monitored  
102 and quantified the microstructural responses during tensile deformation, including the  
103 evolution of lattice strain, stack fault probability and dislocation density versus imposed  
104 strain at both temperatures. The different responses between 293 and 77 K were  
105 compared. We also calculated the stacking fault energy of the alloy at both 293 and 77  
106 K. TEM observations were carried out on the deformed samples, providing correlative  
107 analysis. The work provides in-depth micro-mechanistic understanding involving the  
108 complex interaction of stacking faults, twins and dislocations for the studied tHEAs at  
109 cryogenic temperatures, which could pave the way for designing advanced metallic  
110 materials resistant to cryogenic environments.

## 111 **2. Experimental details**

112 The FeCoCrNi high entropy alloy was fabricated by powder metallurgical processes,  
113 which are detailed in Refs. [33, 35], namely, hot extrusion of gas-atomized FeCoCrNi  
114 powders. The alloy has a single fcc structure and the average grain size of the as-  
115 extruded specimen was approximately 35  $\mu\text{m}$ . The mechanical properties and  
116 microstructure of the alloy at room temperature can be found in Ref. [35].

117 *In situ* time-of-flight neutron diffraction measurements during tensile deformation were  
118 performed on the ENGIN-X neutron diffractometer, Rutherford Appleton Laboratory  
119 (RAL), ISIS, UK [36, 37]. A stress rig with a load capability of 100 kN was used for  
120 the experiments. An in-house built cold chamber, integrated with the stress rig, was  
121 used which provides a controlled cryogenic temperature environment (10-293 K) [38].

122 A schematic of the setup is shown in Fig. 1a. A low temperature extensometer was used  
123 to measure the displacement of the part of gauge length (10 mm). The rig was mounted  
124 on the diffractometer horizontally. The loading axis was oriented horizontally, parallel  
125 to the extruded direction and orientated  $45^\circ$  relatives to the incident beam. The two  
126 detectors (axial and radial) allow collection of the diffraction patterns at fixed  
127 horizontal scattering angles of  $\pm 90^\circ$ , with diffraction vectors parallel and perpendicular  
128 to the loading direction, respectively.

129 Dog bone-shaped uniaxial tensile specimens with a gauge length of 34.5 mm and  
130 diameter of 8 mm were prepared from the as-extruded material. A  $4 \times 4 \times 4 \text{ mm}^3$  neutron  
131 measurement gauge volume was used. Diffraction patterns were acquired for 20 min  
132 intervals between tensile loading steps, iterating until the sample failed. During the  
133 cooling down process for the cryogenic temperature deformation test, a stress level of  
134 5 MPa was maintained via stress-control. During loading up, a stress-control was used  
135 before the yielding point, which was followed by strain-control. The diffraction spectra  
136 was analysed by Open G software which provides the information of d-spacing, peak  
137 intensity and full width at half maximum (FWHM).

138 In order to calculate the stacking fault energy and dislocation density from the measured  
139 diffraction spectra, single peak fitting with a pseudo-voigt convolution was developed  
140 in Matlab. The measured diffraction patterns, after being deconvoluted with the  
141 instrument function, can be described by the convolution of a Gaussian and a Lorentz  
142 function.

$$I(x) = I(0) \left[ \mu \exp \left[ -\pi \frac{(x - x_0)^2}{\beta_G^2} \right] + (1 - \mu) \frac{1}{\frac{\beta_C^2}{\pi^2} + (x - x_0)^2} \right] \quad (1)$$

143 where  $x_0$  is the peak centre, and  $\beta_G$  and  $\beta_C$  are constant parameters of the Guassian and  
 144 Lorentz respectively.  $\mu$  and  $(1-\mu)$  denote the fraction of Guassian and Lorentz used. The  
 145 size strain and microstrain contribution are then related to the parameters of the  
 146 Gaussian and Lorentz function by

$$D_{eff} = \frac{1}{\beta_C} \quad (2)$$

147 And

$$\langle \xi^2 \rangle_{hkl}^{1/2} = \left( \frac{2}{\pi} \right)^{1/2} \beta_G d_{hkl} / 2 \quad (3)$$

148 respectively.  $D_{eff}$  is the effective dimension of coherently diffraction blocks (e.g. grains)  
 149 and  $\xi$  is the microstrain and its root-mean-square could be interpreted to be proportional  
 150 to the square root of dislocation density ( $\rho^{1/2}$ ) as follows:

$$\rho = \frac{k \langle \xi^2 \rangle}{F b^2} \quad (4)$$

151 where  $b$  represents the magnitude of Burgers vector.  $F$  and  $k$  are two constants, and  $F$   
 152 =1 and  $k = 1.61\text{nm}$  were chosen according to [39] for fcc crystal with a Burgers vector  
 153 along  $\langle 110 \rangle$ .

154 Transmission electron microscopy (TEM) study was conducted on a JEOL-2100 TEM  
 155 operated at 200 kV to examine the microstructure of the specimens after the *in situ*  
 156 neutron diffraction experiments. The TEM samples were extracted from regions close

157 to and away from the fracture surfaces which represent samples with different strain  
158 levels. On the sample deformed at 77 K, TEM foils were extracted from the regions  
159 with cross-section diameters equal to 6.8 mm and 6.24 mm which correspond to  
160 reduction in the cross section area ( $\psi$ ) during the tensile test of 27.8% and 39.2%,  
161 respectively. For sample deformed at 293 K, TEM foils were extracted from the regions  
162 with the cross-section diameters equal to 7.15 and 6.47 mm which correspond to the  
163 reduction in cross section area ( $\psi$ ) during the tensile test of 20.1% and 34.6%,  
164 respectively. The foils extracted were ground down to  $\sim 80 \mu\text{m}$ , then disks of 3 mm  
165 diameter were punched out and twin-jet electro-polished in a solution containing 100  
166 mL  $\text{HClO}_4$  and 900 mL  $\text{CH}_3\text{COOH}$  at approximately  $-10^\circ\text{C}$ .

### 167 **3. Results and discussion**

#### 168 **3.1 Mechanical properties**

169 Fig. 1b shows the true stress-true strain curves of the polycrystalline FeCoCrNi alloy  
170 tensile deformed to fracture at 77 and 293 K. The yield strength (YS) and ultimate  
171 tensile strength (UTS) increase from approximately 260MPa and 980MPa at 273 K to  
172 480MPa and 1725 MPa at 77 K. The total elongation also increases from about 45% to  
173 55% (corresponding to engineering strain of 55% and 72% respectively) as the test  
174 temperature is decreased from 293 to 77 K. This enhancement of strength and ductility  
175 of the tHEA alloys at cryogenic temperatures is also compared to a few selected  
176 previous studies, as summarized in Tab. 1. It can be shown that the yield strength and  
177 UTS often increased 1.5-2 times while the maximum elongation often increased 10-  
178 15% when the deformation temperature was dropped from 293 to 77 K. **The mechanical**

179 properties of FeCoCrNiMo<sub>0.23</sub> alloy at both temperatures are also provided in Table 1  
180 for comparison. It shows that micro-alloying the tHEA with Mo enhances the  
181 mechanical properties.

182 The strain hardening rate (SHR), which represents by the derivative of the true stress  
183 with respect to the true strain, is shown in Fig. 1c as a function of true stress. The area  
184 below the line  $d\sigma/d\varepsilon = \sigma$  reveals the region in which necking is predicted to occur  
185 according to Considre's criterion. The SHRs of the alloy at 77 and 293 K show a similar  
186 trend, whereas two distinguished stages can be found in both curves – rapid drop of the  
187 strain hardening rate at small stress level, then the decrease slows down at higher stress.  
188 The transition points between the two stages are marked in Fig. 1b. The transition point  
189 for room temperature tensile test is at 410 MPa (5.6 %) true stress (strain) level, whereas  
190 at 77 K, it is 682 MPa (6.3 %) true stress (strain). The SHR at 77 K is higher than at  
191 room temperature, which is consistent with other studies [5, 6, 23].

192 In summary, the FeCoCrNi alloy has significantly improved strength, ductility and  
193 strain hardening capability at 77 K than at room temperature. The underlying  
194 mechanisms will be discussed with the help of *in situ* neutron diffraction and correlative  
195 electron microscopies in the following sections.

### 196 3.2 The evolution of lattice strain

197 As shown in Fig. 2, the tHEA is a fcc single phase structure at both 293 and 77 K before  
198 deformation. The lattice parameters at 293 and 77 K are 0.3604 and 0.3563 nm,  
199 respectively, calculated by the average of five diffraction peaks. Cooling the sample to  
200 cryogenic temperature results in the drop of lattice parameter. During the course of

201 deformation at both 293 and 77 K, the tHEA stays as a fcc structure (no additional peaks  
202 belongs to bcc and hcp structure appears), which means that martensite transformation  
203 do not occur in this alloy.

204 The changes in lattice strains can be calculated using

$$205 \quad \varepsilon_{hkl} = \frac{d_{hkl} - d_{hkl}^0}{d_{hkl}^0} \quad (4)$$

206 where  $\varepsilon_{hkl}$  is the lattice strain in the  $\{hkl\}$  grain family,  $d_{hkl}$  is the current sample  
207 lattice spacing and  $d_{hkl}^0$  is the stress-free lattice spacing. The stress-free lattice spacing  
208 was taken from the measurement point at 5 MPa at the temperatures.

209 Elastic lattice strains along the axial and radial directions in grain families having  
210  $\{111\}$ ,  $\{200\}$ ,  $\{220\}$ ,  $\{311\}$  and  $\{222\}$  crystallographic planes during tensile  
211 deformation at 77 and 293K, are shown in Fig. 2a and 2b, respectively. The  
212 uncertainties in the measured internal strains were approximately 30 microstrain [40].

213 Fig. 2a shows that the lattice strains increased with applied stress linearly from 0 to 450  
214 MPa, and then nonlinearly when the applied stress was greater than 450MPa during  
215 tensile loading at 77 K. This is due to the fact that the load transfers from softer grain  
216 families (e.g. 220) to harder grain families (e.g. 200) [33]. The trend of lattice strain  
217 evolution at 293 K is similar to that at 77 K, except the nonlinear transition happened  
218 earlier than that at 77 K (above  $\sim 250$ MPa). Overall, at 77 K, the lattice strain values of  
219 all grain families in the axial direction are larger than at 293 K under similar  
220 deformation level.

221 We determined grain orientation dependent diffraction elastic constants ( $E_{hkl}$ ) and  
222 Poisson's ratios ( $V_{hkl}$ ) through fit linear responses to the purely elastic parts of each  
223 curve in Fig. 2.  $E_{\text{Rietveld}}$  and  $V_{\text{Rietveld}}$  have also determined through preform the Rietveld  
224 fitting of 8 peaks. All these values are listed in Tab. 2. The  $E_{hkl}$  values are very similar  
225 for both temperatures. The  $E_{\text{Rietveld}}$ ,  $V_{\text{Rietveld}}$  and  $V_{hkl}$ , are slightly lower at cryogenic  
226 temperatures than room temperature. Daymond et al. [41] show that the value of  $E_{\text{Rietveld}}$   
227 is very similar to the macroscopic Young's modulus. The current temperature  
228 dependent values of  $E_{\text{Rietveld}}$  are compared with the temperature dependent Young's  
229 moduli of CoCrFeMnNi in Ref. [42] with excellent agreement.

### 230 3.3 Stacking fault probability

231 Before we start analysing the stacking fault probability (SFP), we shall note the  
232 relationship between twins and stacking faults. Upon deformation, passage of Shockley  
233 partial dislocation with Burger vector  $1/6\langle 112 \rangle$  on neighbouring two (111) planes  
234 creates an intrinsic stacking fault, and continuous passage of the partial dislocations on  
235 successive (111) planes creates multi-layer faults forming twin nucleuses; in the end  
236 larger twins can be formed by passage of more partials on neighbouring (111) planes  
237 [43]. For alloys with stacking fault between  $18 < \text{SFE} < 45 \text{ mJ/m}^2$ , twinning is more  
238 favourable to occur with external straining. At SFE values  $< 18 \text{ mJ/m}^2$ , martensite  
239 formation occurs when the molar Gibbs energy of martensitic is negative. This  
240 martensitic transformation takes place either by fcc-hcp, or, for even lower SFE,  
241 martensite formation by fcc-hcp-bcc becomes the favoured transformation mechanism  
242 that affects the further deformation of the material [13]. The fcc to hcp transformation

243 can occur by shifting every two neighboring fcc (111) planes in the [11-2] direction by  
244 a distance of  $a/\sqrt{6}$  (where  $a$  is the lattice parameter), which is realised by the partial  
245 dislocation movements in the (111) planes [14]. When SFE exceeds  $45 \text{ mJ/m}^2$ ,  
246 plasticity and strain hardening are controlled solely by the glide of dislocations [15].

247 Many studies [33, 44-46] have shown that stacking faults, if they occur in fcc crystals,  
248 can change the Bragg scattering positions compared with a fault-free lattice. The peak  
249 position shifts for successive orders of reflections such as {111} and {222} might be  
250 different arising from the structure factor for stacking faults. This can be used to  
251 estimate the stacking fault density in the sample.

252 We plot the lattice strain evolutions of {111} and {222} at axial and radial directions  
253 for 77 and 293 K tensile tests in Fig. 4a and 4b, respectively. The separation of {111}  
254 and {222} lattice strain in the axial direction after certain amount of strain is obvious  
255 for both temperatures, which indicates the formation of stacking faults and possibly  
256 twins in grains whose {hkl}|| plane-normals oriented “parallel” to the loading axis.  
257 Interestingly, at room temperature, the {111} and {222} lattice strain curves in the  
258 radial detector bank, almost overlap for the sample deformed. However, at 77K, the  
259 two lattice strain show distinct difference. The radial detector registers a portion of the  
260 grains whose {hkl}⊥ plane-normals are “perpendicular” to the loading axis. The  
261 results suggest that those grains registered are unfavourable for twinning at room  
262 temperature but form stacking faults and twins at 77 K. In addition, it shows that  
263 twinning and stacking fault formation are strongly orientation-dependent (e.g. grains

264 with {hkl}|| plane-normal oriented “parallel” to the loading axis are easier to form  
 265 stacking faults and twins). At cryogenic temperature, twin nucleation and growth can  
 266 be triggered in grains whose orientation is unfavourable for twinning at room  
 267 temperatures.

268 Both (hkl) dependent macro-strain ( $\epsilon_{hkl}^{strain}$ ) and stacking faults ( $\epsilon_{hkl}^{sf}$ ) can contribute to  
 269 the change of lattice strain ( $\epsilon_{hkl}^{exp}$ ) measured by the peak shift in the experiment. The  
 270 measured lattice strain ( $\epsilon_{hkl}^{exp}$ ), (hkl) dependent macro-strain ( $\epsilon_{hkl}^{strain}$ ) and stacking  
 271 faults ( $\epsilon_{hkl}^{sf}$ ) follow a relationship:

$$\epsilon_{hkl}^{exp} = \epsilon_{hkl}^{strain} - \epsilon_{hkl}^{sf} = \epsilon_{hkl}^{strain} - \frac{\sqrt{3}}{4\pi} \frac{\sum_b \pm(h+k+l)}{(u+b)(h^2+k^2+l^2)} SFP \quad (7)$$

272 where  $u$  and  $b$  are the numbers of non-broadened and broadened component due to  
 273 stacking faults; SFP represents stacking fault probability. With the help of Eq. (7), we  
 274 are able to calculate the stacking fault probability, which directly indicates the density  
 275 of stacking faults.

276 The evolution of the stacking fault probability during loading up at 77 and 293 K  
 277 obtained from Eq. 7 are shown in Fig. 4a and 4b. At 77 K, the SFP increases from 0 to  
 278  $3 \times 10^{-3}$  after true strain reaches approximately 4.8%. After this, the SFP increases  
 279 almost linearly with the increase of true strain, especially after the true strain is larger  
 280 than 10%. The SFP increases to  $25.6 \times 10^{-3}$  at the strain level of 47% (close to failure).  
 281 At 293 K, the SFP fluctuates below 0 when the true strain is smaller than 10%. After

282 10% true strain, the SFP becomes positive and increases with true strain steadily up to  
283  $5.4 \times 10^{-3}$  at the strain level of 48.6%, which is about five times smaller than that at 77  
284 K. The evolutions of SFP with applied true strains for both temperatures can be fitted  
285 with a linear function in the true strain range from 3% to 55% (Fig. 4a and 4b). The  
286 slope at 77 K is 0.72, which is about three times larger than that at 293K (0.24).

287 The fact that at 77 K, compared to room temperature, the sample shows much higher  
288 SFP at similar strain level and the SFP curve is much steeper, suggests that at low  
289 temperatures, the FeCoCrNi alloy can form more stacking faults in the sample and the  
290 nucleation and growth of twins might be much quicker than at room temperature.

291 We then plot the SFP as a function of true stress of the FeCoNiCr and FeCoNiCrMo<sub>0.23</sub>  
292 at both 77 and 293 K, as shown in Fig. 4c. For both alloys, the SFP values of the two  
293 deformation temperatures almost overlap at the same stress level when the true stress  
294 is over roughly 450 MPa. This implies that the density of stacking faults of tHEAs is  
295 mainly a function of stress levels, regardless of deformation temperature.  
296 FeCoNiCrMo<sub>0.23</sub> alloy shows similar behaviour. At the same stress, the alloy with Mo  
297 addition has a slightly higher SFP.

### 298 3.4 Stacking fault energy

299 The stacking fault energy (SFE) represents the easiness of dissociating a perfect  
300 dislocation into two partial dislocations and the tendency for the formation of SFs. It  
301 can be calculated by Reed and Schramm's equation [47]. Note that the SFE we

302 measured here by neutron diffraction is the so-called intrinsic stacking fault energy  
303 ( $\gamma_{ISF}$ ).

$$\gamma_{ISF} = \frac{6.6a_0}{\pi\sqrt{3}} \left( \frac{2c_{44}}{c_{11} - c_{12}} \right)^{-0.37} \frac{\langle \xi^2 \rangle_{111}}{SFP} \left( \frac{c_{44} + c_{11} - c_{12}}{3} \right) \quad (8)$$

304 where,  $\gamma_{ISF}$  is the intrinsic stacking fault energy,  $a_0$  is the lattice parameter.  
305  $\langle \xi^2 \rangle_{111}$  is the mean square microstrain, which is obtained by an integral breadth  
306 method with a pseudo-voigt convolution [48]. The single crystal elastic constants  
307 (SCEC) ( $C_{11}=271.0$  GPa,  $C_{12} = 175.0$  GPa, and  $C_{44}=189.3$  GPa) are adopted from *ab*  
308 *initio* atomistic simulation on an fcc FeCoNiCr alloy at 0 K [49]. The SCEC varies only  
309 slightly between 77 K and room temperature according to the simulation work [25].  
310 The stacking fault probability is measured at around engineering strain level of 48% for  
311 both temperatures. The SFE of the FeCoCrNi high-entropy alloy is then estimated by  
312 Eq. 8 to be 13 mJ/m<sup>2</sup> at 77 K and 32.5 mJ/m<sup>2</sup> at 293 K (Tab. 3). Expression (8),  
313 however, is still approximate and we cannot determine reliable error values. There are  
314 likely errors related to the calculation of the mean square micro-strain. Also, the  
315 variation of SCEC between different temperatures and the measurement of SCEC by  
316 atomistic simulation is not taken into account and may add additional uncertainty in the  
317 estimated SFE due to many assumptions included in the model [49]. However,  
318 measurements of SCEC is very limited and we would expect that accurately measuring  
319 SCEC, both by experiments and simulation as a function of temperature, will provide  
320 a more robust determination of SFE using eq. 8. We also estimated the SFE of a

321 FeCoNiCrMo<sub>0.23</sub> to be 19 mJ/m<sup>2</sup> at room temperature [33] and 10 mJ/m<sup>2</sup> at 77 K (Table  
322 3), which is lower than that of the FeCoNiCr alloy, suggesting that micro-alloying of  
323 Mo can reduce the stacking fault energy of the tHEAs.

324 The estimated SFE at room temperature (32.5 mJ/m<sup>2</sup>) agrees with the experimental  
325 measurement on FeCoCrNi tHEA by the combined use of XRD and DFT simulation  
326 (e.g. 17.4, 34.3 and 31.7 mJ/m<sup>2</sup> depending on alloy composition used [50]) and TEM  
327 (27±4 mJ/m<sup>2</sup> [19]). Currently no experimental measurement of tHEAs' SFE at  
328 cryogenic temperature is reported. Only a few simulations were performed on  
329 FeCoNiCr alloy. Zhao *et al.* performed ab initio calculation on a series of fcc tHEAs.  
330 Their results show that the SFE of FeCoNiCr stays negative at 0 K. Depending on which  
331 models they used, the predicted SFE values vary around -20 mJ/m<sup>2</sup> [19] ). Zhang *et al.*  
332 [26] reported that SFE at 0 K of fcc FeCoNiCr falls from -82 to -180 mJ/m<sup>2</sup>. Beyramali  
333 Kivvy and Asle Zaeem's simulation gives a SFE value of 31.6±0.9 mJ/m<sup>2</sup> [19] although  
334 the temperature at which the simulation was carried out is not reported. Our estimation  
335 of SFE at 77 K may provide a validation for SFE simulations if one can carry out the  
336 *ab initio* calculations at different temperatures such as the one performed by Huang *et*  
337 *al.* on a FeCrCoNiMn alloy [25]. Their work obtains an SFE of 8 mJ/m<sup>2</sup> at 77 K on  
338 FeCrCoNiMn alloy, which is slightly lower than our measurement on the FeCrCoNi  
339 alloy, indicating that variations in Mn contents can cause a change to SFE values.

340 The SFE is a critical parameter in the deformation properties of fcc metals and alloys.  
341 The SFE influences phenomena such as the capacity of a dislocation to cross slip, the

342 formation of partial dislocation and twin boundaries [51]. Low SFE can lead to the  
343 domination of a highly planar slip on a well-defined (111) plane, suppressing  
344 dislocation cross-slip, hence augmenting the yield strength [51]. Additionally, Norihiko  
345 *et al.* [52] suggest that the increase of yield stress at cryogenic temperature of tHEAs is  
346 due to the thermal component of solid-solution hardening. The increase of yield stress  
347 at cryogenic temperature is due to both the thermal component of solid-solution  
348 hardening and the suppression of dislocation cross-slip. The very low SFE of the tHEA  
349 used in this study strongly supports the conclusion from section 3.3 that the alloy is  
350 prone to form twins when strained. Additionally, the drop of SFE at cryogenic  
351 temperatures suggests that more deformation twins are able to nucleate and grow when  
352 deformed at lower temperatures.

### 353 **3.5 Critical stress for twinning ( $\sigma_{tw}$ )**

354 Experimental determination of  $\sigma_{tw}$  is challenging. It has been obtained via identifying  
355 the transition point in the work hardening curve [53], or through careful TEM  
356 observation on interrupted strained specimens [23, 35]. The critical stress for twinning  
357 was measured by a few studies using TEM previously, which demonstrates that the  
358 critical stress for twinning was independent of temperature and estimated to be  $\sim 720 \pm 30$   
359 for FeCrNiCoMn alloy [35] and  $790 \pm 100$  MPa for CrCoNi alloy [23]. The criteria used  
360 in those studies for determining the critical twinning stress level is that nano-twins start  
361 to be identified by TEM.

362 As we noted before, the stacking fault probability we measured is directly related to the  
363 density of stacking faults. Hence the SFP curve might allow us to estimate critical points  
364 of stacking fault and twinning formation. The SFP stays negative at very low strains,  
365 and when it reaches over 0, it increases continuously as we increase deformation. The  
366 first critical point we identify is when the stacking fault probability becomes positive  
367 (just above 0). We use the linearly fitted equations (Fig. 4) to determine the stress level  
368 at SFP=0, which are  $450\pm 30$  MPa/9.6% strain at 77K and  $500\pm 15$  MPa/0.717% strain  
369 at 293 K. This point might mark the nucleation stage of stacking fault within the sample  
370 as when stacking faults start to form, the peak positions of the (111) and (222) planes  
371 begin to shift apart, reflecting the contribution from the stacking fault. However, due to  
372 the large scattering of the SFP at lower strain levels, those values should be used with  
373 cautions.

374 The second critical point we consider is when SFP = 0.003 (the purple line in Fig. 4a  
375 and 4b), at which sufficient and sizable stacking faults should have formed, lead to the  
376 nucleation of twin faults. The corresponding true stress values are  $730\pm 30$  MPa/21.2%  
377 strain at 293 K and  $635\pm 30$  MPa/4.885% strain at 77 K (Table 3). The measurement is  
378 consistent with previous studies using TEM [23, 35], suggesting that the SFP curve  
379 could be a reliable way to measure the critical stress for twinning.

380 With regards to the twinning stress prediction, two approaches have been developed.  
381 The classic approach, based on theories such as Venables' pole mechanism [54] and  
382 the Manajan-Chin stacking fault process [55], predicts that the critical resolved shear

383 stress for twinning ( $\tau_{twin}$ ) is proportional to intrinsic stacking fault energy ( $\gamma_{isf}$ ) [53]  
384 ( $\tau_{twin} \times b_p \sim \gamma_{isf}$ ). Based on this, various equations have been formulated, and we  
385 choose a few as shown in Table 4, together with the twinning stress values predicted  
386 based on the equations. The predicted twinning stress values seem to be temperature  
387 dependent. A significant discrepancy among different equations can also be observed.  
388 The huge variations of twinning stress among different models demonstrate that a  
389 systematic validation of the models with experiments is critically needed. Narita and  
390 Takamura's and Venable's models predict relatively low  $\sigma_{tw}$ . It is even lower than the  
391 yield strength at 77 K. Byun's model, on the other hand, gives relatively high values.  
392 According to Byun's model, a twinning stress of 1353 MPa is needed to prompt  
393 deformation twin at room temperature, which is above the UTS of the alloy. If this is  
394 the case, deformation twinning is very unlikely to form during room temperature  
395 deformation, unless some grains experience significant stress concentration. This is in  
396 contradiction with our TEM observation (TEM confirms the formation of nano-twins  
397 within the tensile strained sample, section 3.8). It has been suggested that Byun's model  
398 overestimates the twinning stress in TWIP steels [53], which seems to be the case  
399 according to our result. The twinning stresses predicted by Steinmetz *et al.* model (661  
400 MPa at 77K, 799 MPa at 293 K) seems to agree reasonably well with the twinning stress  
401 values we determined from the SFP curves (635 MPa at 77K, 730 MPa at 293 K).  
402 Steinmetz *et al.* model, based on Mahajan-Chin three-layer twinning mechanism, has  
403 also been shown to accurately predict the twinning stress in TWIP steels [53].

404 It has been suggested that intrinsic SFE alone is not sufficient to predict deformation  
405 twinning mechanisms [53]. The generalized planar fault energy concept, recently  
406 developed, has proposed that the stacking fault formation and twinning process are  
407 controlled by the energy barriers, rather than just the intrinsic stacking fault energy. The  
408 energy barriers include the intrinsic stacking fault energy, the unstable stacking fault  
409 energy, the extrinsic stacking fault energy and the unstable twin fault energy [53]. The  
410 twinning stress is then directly correlated to the unstable twinning fault energy, together  
411 with the intrinsic stacking fault energy. However, to determine the unstable twinning  
412 fault energy by experiments is not possible, and it usually requires using first principle  
413 calculation. Hence, to accurately determine the critical twinning stress, *ab initio*  
414 calculation needs to be performed, which should be validated against the experimental  
415 values via the combined use of interrupted TEM investigation [23, 35] and *in situ*  
416 diffraction methods as demonstrated here.

### 417 **3.6 Evolution of dislocation density**

418 The higher strain hardening rate at 77 K could result from the high dislocation density  
419 in fcc matrix as well as the interaction between dislocations and nano-twins. Here, the  
420 dislocation density during tensile deformation at 77 and 293 K are measured using Eq.  
421 3, which are shown in Fig. 5a as a function of true strain. It indicates that the dislocation  
422 density increases as the strains/stress increases. At the cryogenic temperature, a much  
423 higher density of dislocations is accumulated after plastic deformation. A linear

424 equation ( $\rho = \rho_0 + K\varepsilon$ ) can be used to describe the dislocation density and true strain  
425 relationship:

$$\rho = 1.4 \times 10^{15} + 7.6 \times 10^{13}\varepsilon \quad (10)$$

$$\text{and } \rho = 1.5 \times 10^{15} + 3.5 \times 10^{13}\varepsilon \quad (11)$$

426 at 77 and 293 K, respectively.

427 The increases in the tensile stress,  $\Delta\sigma$ , due to forest dislocation interactions can be  
428 described by:

$$\Delta\sigma = \alpha M G b \rho^{1/2} \quad (12)$$

429 where  $\alpha$  is a constant,  $M$  is the Taylor factor (3.06),  $G$  is the shear modulus (85 GPa  
430 at 77 K; 80 GPa at 293K [42, 56]),  $b$  is the magnitude of the Burgers vector  
431 (0.252 nm at 77 K and 0.253 nm at 293 K) and  $\rho$  is the dislocation density. Fig. 5b  
432 shows the normalized increment of stresses  $(\sigma - \sigma_y)/MG$  (where  $\sigma$  is the current stress)  
433 at both 77 and 293 K, which can be fitted with a linear function. Only data beyond the  
434 yielding is included. The slope of the linear function at 77 K is 0.53 which agrees with  
435 that found in CrMnFeCoNi [6]. The slope of the linear function at 293 K is 0.95, which  
436 almost doubles the value at 77 K. However, we note that the physical meaning of  $\alpha$  is  
437 not very clear hence it is hard to interpret, and Eq. 12 ignores the contribution from the  
438 other sources including dislocation-mechanical twin boundary interaction.

439 Gini *et al.* [57] proposed an equation that incorporates Eq. 12 and the plasticity model  
440 of Nes and Marthinsen [58]:

$$\Delta\sigma = \alpha M G b \rho^{1/2} + \frac{M \beta G b}{\Lambda} \quad (13)$$

441 where  $\Lambda$  is the dislocation mean free path, and  $\beta$  is a constant. The formation of  
442 mechanical twins reduces the dislocation mean free path. Thereby, according to Eq.13,  
443 it is the dynamic increase of boundaries, due to the formation of mechanical twinning,  
444 together with the continuously increase of dislocation density that leads to the enhanced  
445 strain hardening behaviour of the tHEA during plastic deformation.

### 446 **3.7 Peak intensity**

447 Fig. 6 also shows the normalized peak intensity evolution of several lattice reflections  
448 parallel and perpendicular to the load axis versus true stress. A few points can be drawn  
449 regarding the changes of peak intensity and the differences at 77 and 293K:

450 (i) The peak intensity of the axial (220) decreased significantly when the applied  
451 load was larger than the macroscopic yielding, as shown in Fig. 6. The (220)  
452 peak at axial direction almost vanished when the applied stress was above 1500  
453 MPa at 77 k and 800 MPa at 293 K. The fact that the (220) peak disappears  
454 when the sample is strained close to failure in both samples is very interesting  
455 and has been observed before in a FeCoNiCrMo<sub>0.23</sub> alloy as well. In contrast,  
456 the peak intensity of 220 at radial direction increased by a factor of 1.1 to 2  
457 during the whole deformation.

458 (ii) The peak intensity of (200) at both axial and radial directions increased  
459 significantly at 77 K, but hardly changed at 293K.

460 (iii) For (111) and (222) grains families, the peak intensity increased in axial  
461 direction by a factor of 3 at 77 K but decreased in radial direction. The final  
462 peak intensity of (222) and (111) changed by a factor of ~5.5 at 293 K.

463 Significant difference in peak intensity evolution at 77 and 293 K was observed,  
464 signifying the different behaviour in terms of the re-orientation of grains during the  
465 tensile deformation, which could be due to slip/rotation of grains [59] and/or formation  
466 of mechanical twins [60]. However, it is not easy to distinguish the contribution from  
467 grain rotation and mechanical twins.

### 468 **3.8 Microstructure characterisation**

469 The microstructures of the deformed specimens after the *in situ* neutron studies were  
470 analysed by transmission electron microscopy (TEM) in order to gain a better  
471 understanding of the controlling deformation mechanisms. TEM bright field (BF)  
472 images and selected area diffraction patterns (SADP) of the samples deformed at 77  
473 and 293 K are shown in Figs. 7 and 8, respectively, showing that nano-sized lamellas  
474 have formed to accommodate strain when the sample was deformed at both  
475 temperatures. The lamellas are twin structure as confirmed by the diffraction patterns  
476 in Fig. 7d and 8d. TEM samples for Fig. 7a and 7b are taken from the failed *in situ*  
477 samples at different reductions in cross-section area ( $\psi$ ). The twin-twin intersections  
478 can also be readily observed in Fig. 7a and 7b, which can form a complex 3-dimensional  
479 network inhibiting dislocation propagation. Fig. 7a and 7b also show that at 77 K more

480 twins are formed at higher strain level. Comparing Fig. 7 with Fig.8, we conclude that  
481 less twins and twin-twin intersections are formed at room temperature, consistent with  
482 our measurement from *in situ* neutron diffraction. We do not observe martensite phase  
483 at both temperature through TEM, again, consistent with our observation by neutron  
484 diffraction (Fig. 2). A further drop of deformation temperature might lead to the  
485 formation of martensite as SFE will become ever lower.

486 The dramatic increase of nano-twins and twin-twin intersections at lower temperatures  
487 plays a key role for the higher strain hardening ability the alloy achieved at 77 K than  
488 293 K as shown in Fig. 1b. The combination of enhanced dislocation hardening (higher  
489 dislocation density during cryogenic deformation) and mechanical twinning (higher  
490 twin volume fraction during cryogenic deformation) provide a larger work hardening  
491 rate during tensile deformation at 77 K than at 293 K.

#### 492 **4. Conclusions**

493 In our work, we fabricated a FeCoNiCr high entropy alloy with a single phase fcc  
494 structure using a powder metallurgy route. We used *in situ* neutron diffraction to map  
495 the evolution of deformation microstructure at both 77 and 293 K, correlatively  
496 characterized by TEM. Several conclusions can be drawn based on the experimental  
497 results:

- 498 1. The alloy has a good combination of high ultimate tensile strength (UTS ~1725  
499 MPa) and ductility (elongation~55%) at 77 K, which is much higher than the  
500 room temperature properties (UTS ~ 980 MPa, and elongation ~45%). Higher

501 strain hardening rate is also obtained at cryogenic temperature than at room  
502 temperature.

503 2. Via *in situ* neutron diffraction measurement, we are able to determine the  
504 stacking fault probability (SFP) as a function of stress level at both 77 and 293  
505 K. The SFP increases much quicker and reaches a much higher value at similar  
506 strain levels at cryogenic temperature than room temperature.

507 3. Using diffraction line profile analysis, stacking fault energy is estimated to be  
508  $\sim 13 \text{ mJ/m}^2$  at 77 K and  $\sim 32.5 \text{ mJ/m}^2$  at 293 K. As the SFE drops at cryogenic  
509 temperature, more twin faults form as the alloy is deformed at cryogenic  
510 temperatures. Nano-twins at both 77 and 293 K of the alloy have been observed  
511 by TEM, and at 77 K, many more twins and twin-twin intersections are formed  
512 than at room temperature.

513 4. We used the stacking fault probability curve to determine the critical stress for  
514 twinning. The critical stress for twinning is set to stress levels when the SFP is  
515 0.003. The corresponding true stress values are  $730 \pm 30 \text{ MPa}$  at 293 K and  
516  $635 \pm 30 \text{ MPa}$  at 77 K, which agree with previous measurements on  
517 CrCoNi and CrMnFeCoNi alloys as well as Steinmetz *et al.* model.

518 5. Dislocation density is calculated for both temperatures from neutron diffraction  
519 spectra. Higher dislocation density is found during low temperature plastic  
520 deformation than at room temperature.

521 6. The combination of dislocation hardening and mechanical twinning provides  
522 large work hardening rate and high strength during tensile deformation for the  
523 high entropy alloy. The superior mechanical properties at the cryogenic  
524 temperature is attributed to the enhanced dynamic Hall-Petch hardening and  
525 dislocation hardening as at lower temperatures, increased amount of nano-twins  
526 and dislocation are formed.

### 527 **Acknowledgements**

528 The authors thank ISIS (the Rutherford Appleton Laboratory, UK) for providing the  
529 beamtime (RB1610297) and staff at EnginX beamline for support. Y.Q.W. and P.D.L.  
530 acknowledge the support provided by the Research Complex at Harwell, funded in part  
531 by EPSRC ((EP/K007734/1 and EP/L018705/1).. B.C. acknowledges the support from  
532 Diamond Birmingham Collaboration. Y.L. and B.L. acknowledge the National Natural  
533 Science Foundation of China (51671217), and the Projects of Innovation-driven Plan  
534 in Central South University of China (2015CX004).

535 **Tables**

536 Table 1. Comparison of yield strength (YS), ultimate tensile strength (UTS), and total  
 537 elongation obtained at 77K and 293K from the present study to selected prior studies.  
 538

Materials	Temp. (K)	YS (MPa)	UTS (MPa)	Elongation (%)
FeCoCrNi	77	480	1725	55
	293	260	980	45
FeCoCrNiMo <sub>0.23</sub>	77	602	1863	51
	293	360	1238	48
CrCoNi [23]	77	560	1625	44
	293	360	750	30
CrMnFeCoNi [6]	77	460	1060	60
	293	265	600	45

539

540

541  
542  
543  
544

Table 2. Uniaxial materials properties of FeCoCrNi HEA at 77 and 293 K

Temp.	a	E <sub>111</sub>	E <sub>200</sub>	E <sub>220</sub>	E <sub>311</sub>	E <sub>Rietveld</sub>	V <sub>111</sub>	V <sub>200</sub>	V <sub>220</sub>	V <sub>311</sub>	V <sub>Rietveld</sub>
(K)	(nm)	(GPa)	(GPa)	(GPa)	(GPa)	(GPa)					
77	0.3563	146.3	97.0	191.6	214.0	229	0.138	0.232	0.168	0.234	0.20
293	0.3604	136.6	98.0	175.0	237.2	190	0.198	0.349	0.348	0.321	0.27

545  
546

547

548

549

Table 3. Stacking fault energy of FeCoCrNi tHEA at 77 and 293 K

	FeCoCrNi	FeCoCrNi	FeCoCrNiMo <sub>0.23</sub>	FeCoCrNiMo <sub>0.23</sub>
Temperature	77 K	293 K	77 K	293 K
SFE (mJ/m <sup>2</sup> )	13	32.5	10	19
Twinning Stress	635 ± 30	730 ± 30	-	-

550

551

552

Table 4. Critical stress for twinning of FeCoCrNi tHEA at 77 and 293 K

Sources	Equations	Temp.	$\tau_{tw}$ (MPa)	$\sigma_{tw}$ (MPa)
Narita and Takamura [55]	$\tau_{tw} = \frac{\gamma_{isf}}{2b_p}$	77 K	45	135
		293 K	110	337
Venable [54, 61]	$\tau_{tw} = \frac{b\gamma_{isf}}{b_p(nb - b_p)}$	77 K	37-63	113-193
		293 K	91-155	278-474
Byun [62]	$\tau_{tw} = \frac{2\gamma_{isf}}{b_p}$	77 K	178	545
		293 K	442	1353
Steinmetz <i>et al.</i> [63]	$\tau_{tw} = \frac{\gamma_{isf}}{3b_p} + \frac{3Gb_p}{L_0}$	77K	216	661
		293 K	261	799

553

\*  $n$  is the stress-concentration factor ( $n=1$  represents no stress concentration while  $n \geq 3$  means static tension, here  $n = 2-3$ ) [20];

554

555

\*  $L_0$  is the width of a twin embryo (approximately 200 nm);

556

\*  $\sigma_{tw} = M\tau_{tw}$ , where  $M$  is the Taylor factor.

557

558

559

560

561

562

563

564 **List of figures**

565 Fig. 1. (a) Schematic of the in situ neutron diffraction set-up; (b) True stress-strain  
566 curves of uniaxial tensile tests at 77 K and 293 K and (c) the corresponding working  
567 hardening rate versus true stress.

568 Fig. 2. Diffraction patterns collected at the axial detector as a function of stress at (a)  
569 293 K; and (b) 77 K.

570 Fig. 3. The evolution of elastic lattice strains along the axial and radial directions in  
571 grain families having {111}, {200}, {220}, {311} and {222} crystallographic planes  
572 during tensile loading at (a) 77 K and (b) 293 K;

573 Fig. 4. The (111) first order and (222) second order reflections together with the  
574 stacking fault probability as a function of true strain at (a) 77 K and (b) 293 K.

575 Fig. 5. The evolution of dislocation density versus (a) true strain, and (b) normalised  
576 work hardening  $(\sigma - \sigma_y)/MG$  versus  $b\rho^{1/2}$ .

577 Fig. 6. The evolution of normalized peak intensity along the axial and radial directions  
578 in grain families having {111}, {200}, {220}, {311} and {222} crystallographic planes  
579 during tensile loading at (a) 77 K and (b) 293 K.

580 Fig. 7. TEM bright field micrographs of samples with (a) 27.8 % and (b) 39.2% strain  
581 at 77 K, which show nano-twins. (c) Higher magnification BF images with an inserted  
582 SAD pattern obtained from the matrix and (f) the composite SAD pattern obtained from  
583 the blue circled region in Fig. 7c which has contribution from both the matrix and the  
584 nano-twin.

585 Fig. 8. TEM bright field micrographs of samples with (a) 20.1% and (b) 34.6% strain  
586 at 293k, which show nano-twins. (c) Higher magnification BF images with an inserted  
587 SAD pattern obtained from the matrix and (f) the composite SAD pattern obtained from  
588 the blue circled region in Fig. 8c which has contribution from both the matrix and the  
589 nano-twin.

590

591

592

593

595 **Reference**

- 596 [1] B. Cantor, I. Chang, P. Knight, A. Vincent, Microstructural development in  
597 equiatomic multicomponent alloys, *Materials Science and Engineering: A* 375 (2004)  
598 213-218.
- 599 [2] J.W. Yeh, S.K. Chen, S.J. Lin, J.Y. Gan, T.S. Chin, T.T. Shun, C.H. Tsau, S.Y.  
600 Chang, Nanostructured high-entropy alloys with multiple principal elements: novel  
601 alloy design concepts and outcomes, *Advanced Engineering Materials* 6(5) (2004) 299-  
602 303.
- 603 [3] B. Gludovatz, A. Hohenwarter, D. Catoor, E.H. Chang, E.P. George, R.O. Ritchie,  
604 A fracture-resistant high-entropy alloy for cryogenic applications, *Science* 345(6201)  
605 (2014) 1153-1158.
- 606 [4] F. Otto, A. Dlouhý, C. Somsen, H. Bei, G. Eggeler, E.P. George, The influences of  
607 temperature and microstructure on the tensile properties of a CoCrFeMnNi high-  
608 entropy alloy, *Acta Materialia* 61(15) (2013) 5743-5755.
- 609 [5] J. Moon, S.I. Hong, J.W. Bae, M.J. Jang, D. Yim, H.S. Kim, On the strain rate-  
610 dependent deformation mechanism of CoCrFeMnNi high-entropy alloy at liquid  
611 nitrogen temperature, *Materials Research Letters* (2017) 1-6.
- 612 [6] G. Laplanche, A. Kostka, O. Horst, G. Eggeler, E. George, Microstructure evolution  
613 and critical stress for twinning in the CrMnFeCoNi high-entropy alloy, *Acta Materialia*  
614 118 (2016) 152-163.
- 615 [7] A. Gali, E.P. George, Tensile properties of high-and medium-entropy alloys,  
616 *Intermetallics* 39 (2013) 74-78.
- 617 [8] Z. Li, K.G. Pradeep, Y. Deng, D. Raabe, C.C. Tasan, Metastable high-entropy dual-  
618 phase alloys overcome the strength–ductility trade-off, *Nature* 534(7606) (2016) 227.
- 619 [9] D.T. Pierce, J.A. Jiménez, J. Bentley, D. Raabe, J.E. Wittig, The influence of  
620 stacking fault energy on the microstructural and strain-hardening evolution of Fe–Mn–  
621 Al–Si steels during tensile deformation, *Acta Materialia* 100 (2015) 178-190.
- 622 [10] K. Yan, D.G. Carr, M.D. Callaghan, K.-D. Liss, H. Li, Deformation mechanisms  
623 of twinning-induced plasticity steels: In situ synchrotron characterization and  
624 modeling, *Scripta Materialia* 62(5) (2010) 246-249.
- 625 [11] K. Rahman, V. Vorontsov, D. Dye, The effect of grain size on the twin initiation  
626 stress in a TWIP steel, *Acta Materialia* 89 (2015) 247-257.
- 627 [12] M. Jo, Y.M. Koo, B.-J. Lee, B. Johansson, L. Vitos, S.K. Kwon, Theory for  
628 plasticity of face-centered cubic metals, *Proceedings of the National Academy of*  
629 *Sciences* 111(18) (2014) 6560-6565.
- 630 [13] S. Curtze, V.-T. Kuokkala, Dependence of tensile deformation behavior of TWIP  
631 steels on stacking fault energy, temperature and strain rate, *Acta materialia* 58(15)  
632 (2010) 5129-5141.

633 [14] K. Tao, J.J. Wall, H. Li, D.W. Brown, S.C. Vogel, H. Choo, In situ neutron  
634 diffraction study of grain-orientation-dependent phase transformation in 304L stainless  
635 steel at a cryogenic temperature, *Journal of applied physics* 100(12) (2006) 123515.

636 [15] O. Grässel, L. Krüger, G. Frommeyer, L. Meyer, High strength Fe–Mn–(Al, Si)  
637 TRIP/TWIP steels development—properties—application, *International Journal of*  
638 *plasticity* 16(10-11) (2000) 1391-1409.

639 [16] H. Barman, A. Hamada, T. Sahu, B. Mahato, J. Talonen, S. Shee, P. Sahu, D.  
640 Porter, L. Karjalainen, A Stacking Fault Energy Perspective into the Uniaxial Tensile  
641 Deformation Behavior and Microstructure of a Cr-Mn Austenitic Steel, *Metallurgical*  
642 *and Materials Transactions A* 45(4) (2014) 1937-1952.

643 [17] Y. Tian, L. Zhao, S. Chen, A. Shibata, Z. Zhang, N. Tsuji, Significant contribution  
644 of stacking faults to the strain hardening behavior of Cu-15% Al alloy with different  
645 grain sizes, *Scientific reports* 5 (2015) 16707.

646 [18] X. Xu, P. Liu, Z. Tang, A. Hirata, S. Song, T. Nieh, P. Liaw, C. Liu, M. Chen,  
647 Transmission electron microscopy characterization of dislocation structure in a face-  
648 centered cubic high-entropy alloy Al<sub>0.1</sub>CoCrFeNi, *Acta Materialia* 144 (2018) 107-  
649 115.

650 [19] S. Liu, Y. Wu, H. Wang, J. He, J. Liu, C. Chen, X. Liu, H. Wang, Z. Lu, Stacking  
651 fault energy of face-centered-cubic high entropy alloys, *Intermetallics* (2017).

652 [20] H. Diao, R. Feng, K. Dahmen, P. Liaw, Fundamental deformation behavior in  
653 high-entropy alloys: An overview, *Current Opinion in Solid State and Materials*  
654 *Science* (2017).

655 [21] C.L. Tracy, S. Park, D.R. Rittman, S.J. Zinkle, H. Bei, M. Lang, R.C. Ewing, W.L.  
656 Mao, High pressure synthesis of a hexagonal close-packed phase of the high-entropy  
657 alloy CrMnFeCoNi, *Nature communications* 8 (2017) 15634.

658 [22] F. Zhang, S. Zhao, K. Jin, H. Bei, D. Popov, C. Park, J.C. Neufeind, W.J. Weber,  
659 Y. Zhang, Pressure-induced fcc to hcp phase transition in Ni-based high entropy solid  
660 solution alloys, *Applied Physics Letters* 110(1) (2017) 011902.

661 [23] G. Laplanche, A. Kostka, C. Reinhart, J. Hunfeld, G. Eggeler, E. George, Reasons  
662 for the superior mechanical properties of medium-entropy CrCoNi compared to high-  
663 entropy CrMnFeCoNi, *Acta Materialia* 128 (2017) 292-303.

664 [24] P. Sahu, S. Shee, A. Hamada, L. Rovatti, T. Sahu, B. Mahato, S.G. Chowdhury,  
665 D. Porter, L. Karjalainen, Low strain rate deformation behavior of a Cr–Mn austenitic  
666 steel at– 80° C, *Acta Materialia* 60(20) (2012) 6907-6919.

667 [25] S. Huang, W. Li, S. Lu, F. Tian, J. Shen, E. Holmström, L. Vitos, Temperature  
668 dependent stacking fault energy of FeCrCoNiMn high entropy alloy, *Scripta Materialia*  
669 108 (2015) 44-47.

670 [26] Y. Zhang, Y. Zhuang, A. Hu, J. Kai, C. Liu, The origin of negative stacking fault  
671 energies and nano-twin formation in face-centered cubic high entropy alloys, *Scripta*  
672 *Materialia* 130 (2017) 96-99.

673 [27] Z. Zhang, H. Sheng, Z. Wang, B. Gludovatz, Z. Zhang, E.P. George, Q. Yu, S.X.  
674 Mao, R.O. Ritchie, Dislocation mechanisms and 3D twin architectures generate

675 exceptional strength-ductility-toughness combination in CrCoNi medium-entropy  
676 alloy, *Nature communications* 8 (2017) 14390.

677 [28] S. Zhao, G.M. Stocks, Y. Zhang, Stacking fault energies of face-centered cubic  
678 concentrated solid solution alloys, *Acta Materialia* 134 (2017) 334-345.

679 [29] Z. Zhang, M. Mao, J. Wang, B. Gludovatz, Z. Zhang, S.X. Mao, E.P. George, Q.  
680 Yu, R.O. Ritchie, Nanoscale origins of the damage tolerance of the high-entropy alloy  
681 CrMnFeCoNi, *Nature communications* 6 (2015) 10143.

682 [30] J. Liu, C. Chen, Y. Xu, S. Wu, G. Wang, H. Wang, Y. Fang, L. Meng, Deformation  
683 twinning behaviors of the low stacking fault energy high-entropy alloy: An in-situ TEM  
684 study, *Scripta Materialia* 137 (2017) 9-12.

685 [31] M. Wang, Z. Li, D. Raabe, In-situ SEM observation of phase transformation and  
686 twinning mechanisms in an interstitial high-entropy alloy, *Acta Materialia* 147 (2018)  
687 236-246.

688 [32] L. Ma, L. Wang, Z. Nie, F. Wang, Y. Xue, J. Zhou, T. Cao, Y. Wang, Y. Ren,  
689 Reversible deformation-induced martensitic transformation in Al<sub>0.6</sub>CoCrFeNi high-  
690 entropy alloy investigated by in situ synchrotron-based high-energy X-ray diffraction,  
691 *Acta Materialia* 128 (2017) 12-21.

692 [33] B. Cai, B. Liu, S. Kabra, Y. Wang, K. Yan, P.D. Lee, Y. Liu, Deformation  
693 mechanisms of Mo alloyed FeCoCrNi high entropy alloy: In situ neutron diffraction,  
694 *Acta Materialia* 127 (2017) 471-480.

695 [34] Y. Wu, W. Liu, X. Wang, D. Ma, A.D. Stoica, T. Nieh, Z. He, Z. Lu, In-situ  
696 neutron diffraction study of deformation behavior of a multi-component high-entropy  
697 alloy, *Applied Physics Letters* 104(5) (2014) 051910.

698 [35] B. Liu, J. Wang, Y. Liu, Q. Fang, Y. Wu, S. Chen, C. Liu, Microstructure and  
699 mechanical properties of equimolar FeCoCrNi high entropy alloy prepared via powder  
700 extrusion, *Intermetallics* 75 (2016) 25-30.

701 [36] J. Santisteban, M. Daymond, J. James, L. Edwards, ENGIN-X: a third-generation  
702 neutron strain scanner, *Journal of Applied Crystallography* 39(6) (2006) 812-825.

703 [37] S.Y. Zhang, A. Evans, E. Eren, B. Chen, M. Pavier, Y. Wang, S. Pierret, R. Moat,  
704 B. Mori, ENGIN-X—instrument for materials science and engineering research, *Neutron*  
705 *News* 24(3) (2013) 22-26.

706 [38] O. Kirichek, J. Timms, J. Kelleher, R. Down, C. Offer, S. Kabra, S. Zhang, Sample  
707 environment for neutron scattering measurements of internal stresses in engineering  
708 materials in the temperature range of 6 K to 300 K, *Review of Scientific Instruments*  
709 88(2) (2017) 025103.

710 [39] G. Williamson, R. Smallman, III. Dislocation densities in some annealed and cold-  
711 worked metals from measurements on the X-ray debye-scherrer spectrum,  
712 *Philosophical Magazine* 1(1) (1956) 34-46.

713 [40] Y. Wang, S. Hossain, S. Kabra, S. Zhang, D. Smith, C. Truman, Effect of boundary  
714 conditions on the evolution of lattice strains in a polycrystalline austenitic stainless  
715 steel, *Journal of Materials Science* 52(13) (2017) 7929-7936.

716 [41] M. Daymond, M. Bourke, R. Von Dreele, B. Clausen, T. Lorentzen, Use of  
717 Rietveld refinement for elastic macrostrain determination and for evaluation of plastic

718 strain history from diffraction spectra, *Journal of Applied Physics* 82(4) (1997) 1554-  
719 1562.

720 [42] G. Laplanche, P. Gadaud, O. Horst, F. Otto, G. Eggeler, E. George, Temperature  
721 dependencies of the elastic moduli and thermal expansion coefficient of an equiatomic,  
722 single-phase CoCrFeMnNi high-entropy alloy, *Journal of Alloys and Compounds* 623  
723 (2015) 348-353.

724 [43] S. Kibey, J. Liu, D. Johnson, H. Sehitoglu, Predicting twinning stress in fcc metals:  
725 Linking twin-energy pathways to twin nucleation, *Acta materialia* 55(20) (2007) 6843-  
726 6851.

727 [44] J. Jeong, W. Woo, K. Oh, S. Kwon, Y. Koo, In situ neutron diffraction study of  
728 the microstructure and tensile deformation behavior in Al-added high manganese  
729 austenitic steels, *Acta Materialia* 60(5) (2012) 2290-2299.

730 [45] J. Jeong, Y. Koo, I. Jeong, S. Kim, S. Kwon, Micro-structural study of high-Mn  
731 TWIP steels using diffraction profile analysis, *Materials Science and Engineering: A*  
732 530 (2011) 128-134.

733 [46] J.t. Cohen, C. Wagner, Determination of twin fault probabilities from the  
734 diffraction patterns of fcc metals and alloys, *Journal of Applied Physics* 33(6) (1962)  
735 2073-2077.

736 [47] R. Reed, R. Schramm, Relationship between stacking-fault energy and x-ray  
737 measurements of stacking-fault probability and microstrain, *Journal of Applied Physics*  
738 45(11) (1974) 4705-4711.

739 [48] S. Harjo, Y. Tomota, P. Lukáš, D. Neov, M. Vrana, P. Mikula, M. Ono, In situ  
740 neutron diffraction study of  $\alpha$ - $\gamma$  Fe-Cr-Ni alloys under tensile deformation, *Acta*  
741 *materialia* 49(13) (2001) 2471-2479.

742 [49] F. Tian, L.K. Varga, N. Chen, L. Delczeg, L. Vitos, Ab initio investigation of high-  
743 entropy alloys of 3 d elements, *Physical Review B* 87(7) (2013) 075144.

744 [50] A. Zaddach, C. Niu, C. Koch, D. Irving, Mechanical properties and stacking fault  
745 energies of NiFeCrCoMn high-entropy alloy, *Jom* 65(12) (2013) 1780-1789.

746 [51] J.P. Hirth, J. Lothe, *Theory of dislocations*, (1982).

747 [52] N.L. Okamoto, S. Fujimoto, Y. Kambara, M. Kawamura, Z.M. Chen, H.  
748 Matsunoshita, K. Tanaka, H. Inui, E.P. George, Size effect, critical resolved shear  
749 stress, stacking fault energy, and solid solution strengthening in the CrMnFeCoNi high-  
750 entropy alloy, *Scientific reports* 6 (2016) 35863.

751 [53] B.C. De Cooman, Y. Estrin, S.K. Kim, Twinning-induced plasticity (TWIP) steels,  
752 *Acta Materialia* 142 (2018) 283-362.

753 [54] J. Venables, Deformation twinning in face-centred cubic metals, *Philosophical*  
754 *magazine* 6(63) (1961) 379-396.

755 [55] N. Naeita, J. Takamura, Deformation twinning in silver-and copper-alloy crystals,  
756 *Philosophical Magazine* 29(5) (1974) 1001-1028.

757 [56] A. Haglund, M. Koehler, D. Catoor, E. George, V. Keppens, Polycrystalline elastic  
758 moduli of a high-entropy alloy at cryogenic temperatures, *Intermetallics* 58 (2015) 62-  
759 64.

760 [57] G. Dini, R. Ueji, A. Najafizadeh, S. Monir-Vaghefi, Flow stress analysis of TWIP  
761 steel via the XRD measurement of dislocation density, *Materials Science and*  
762 *Engineering: A* 527(10) (2010) 2759-2763.

763 [58] E. Nes, K. Marthinsen, Modeling the evolution in microstructure and properties  
764 during plastic deformation of fcc-metals and alloys—an approach towards a unified  
765 model, *Materials Science and Engineering: A* 322(1) (2002) 176-193.

766 [59] W. Woo, E.-W. Huang, J.-W. Yeh, H. Choo, C. Lee, S.-Y. Tu, In-situ neutron  
767 diffraction studies on high-temperature deformation behavior in a CoCrFeMnNi high  
768 entropy alloy, *Intermetallics* 62 (2015) 1-6.

769 [60] D. Brown, M. Bourke, M. Stout, P. Dunn, R. Field, D. Thoma, Uniaxial tensile  
770 deformation of uranium 6 wt pct niobium: a neutron diffraction study of deformation  
771 twinning, *Metallurgical and Materials Transactions A* 32(9) (2001) 2219-2228.

772 [61] J.W. Christian, S. Mahajan, Deformation twinning, *Progress in materials science*  
773 39(1-2) (1995) 1-157.

774 [62] Y.-F. Shen, Y. Wang, X.-P. Liu, X. Sun, R.L. Peng, S.-Y. Zhang, L. Zuo, P.K.  
775 Liaw, Deformation mechanisms of a 20Mn TWIP steel investigated by in situ neutron  
776 diffraction and TEM, *Acta Materialia* 61(16) (2013) 6093-6106.

777 [63] D.R. Steinmetz, T. Jäpel, B. Wietbrock, P. Eisenlohr, I. Gutierrez-Urrutia, A.  
778 Saeed-Akbari, T. Hickel, F. Roters, D. Raabe, Revealing the strain-hardening behavior  
779 of twinning-induced plasticity steels: Theory, simulations, experiments, *Acta*  
780 *Materialia* 61(2) (2013) 494-510.

781

782

783

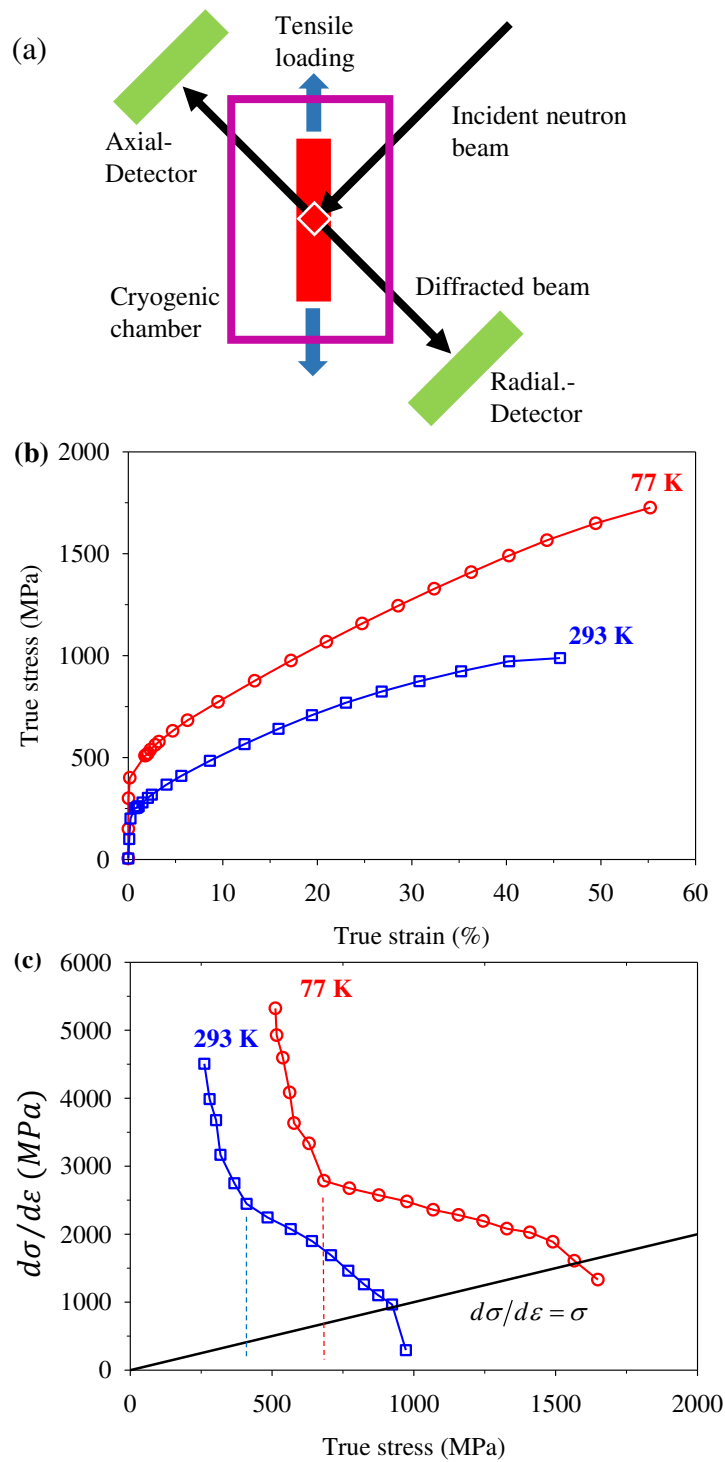


Fig. 1. (a) Schematic of the *in situ* neutron diffraction setup; (b) True stress-strain curves of uniaxial tensile tests at 77 K and 293 K and (c) the corresponding work hardening rate versus true stress.

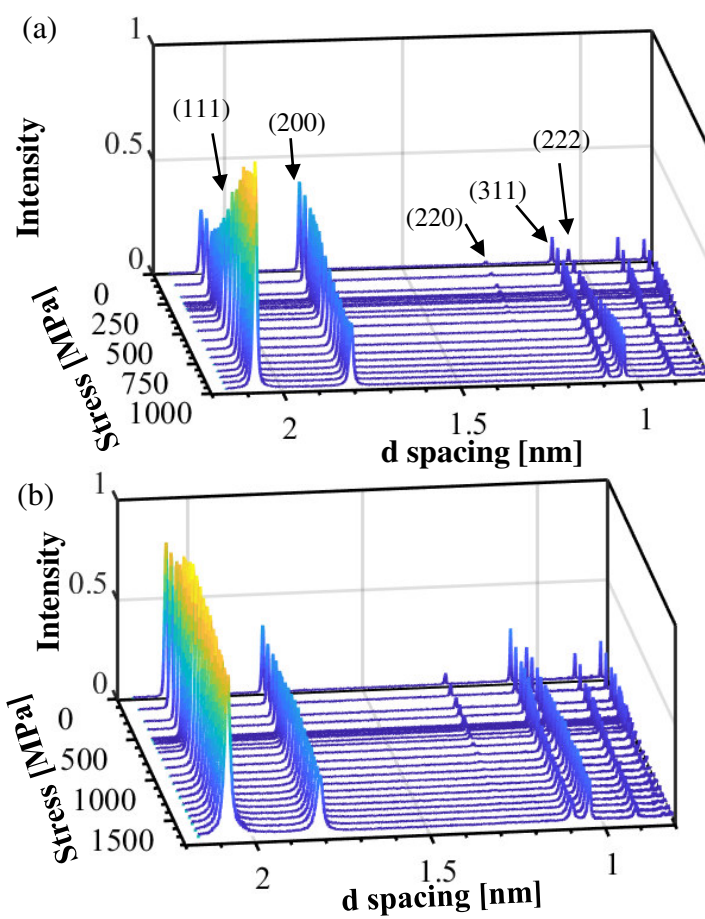


Fig. 2. Diffraction patterns collected at the axial detector as a function of stress at (a) 293 K; and (b) 77 K.

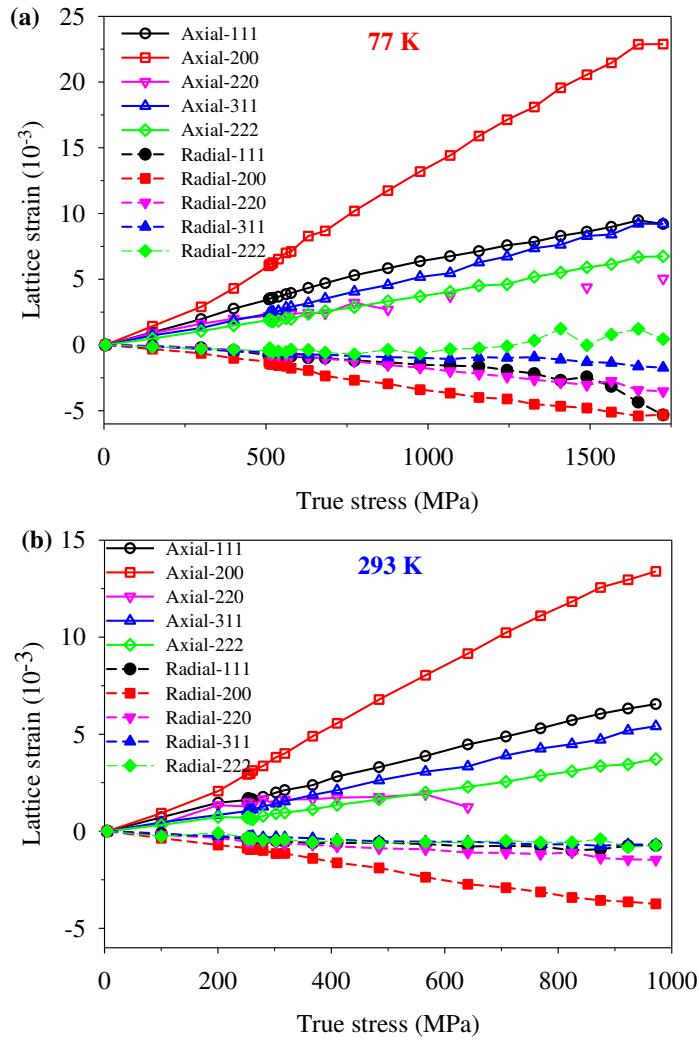


Fig. 3. The evolution of elastic lattice strains along the axial and radial directions in grain families having  $\{111\}$ ,  $\{200\}$ ,  $\{220\}$ ,  $\{311\}$  and  $\{222\}$  crystallographic planes during tensile loading at (a) 77 K and (b) 293 K;

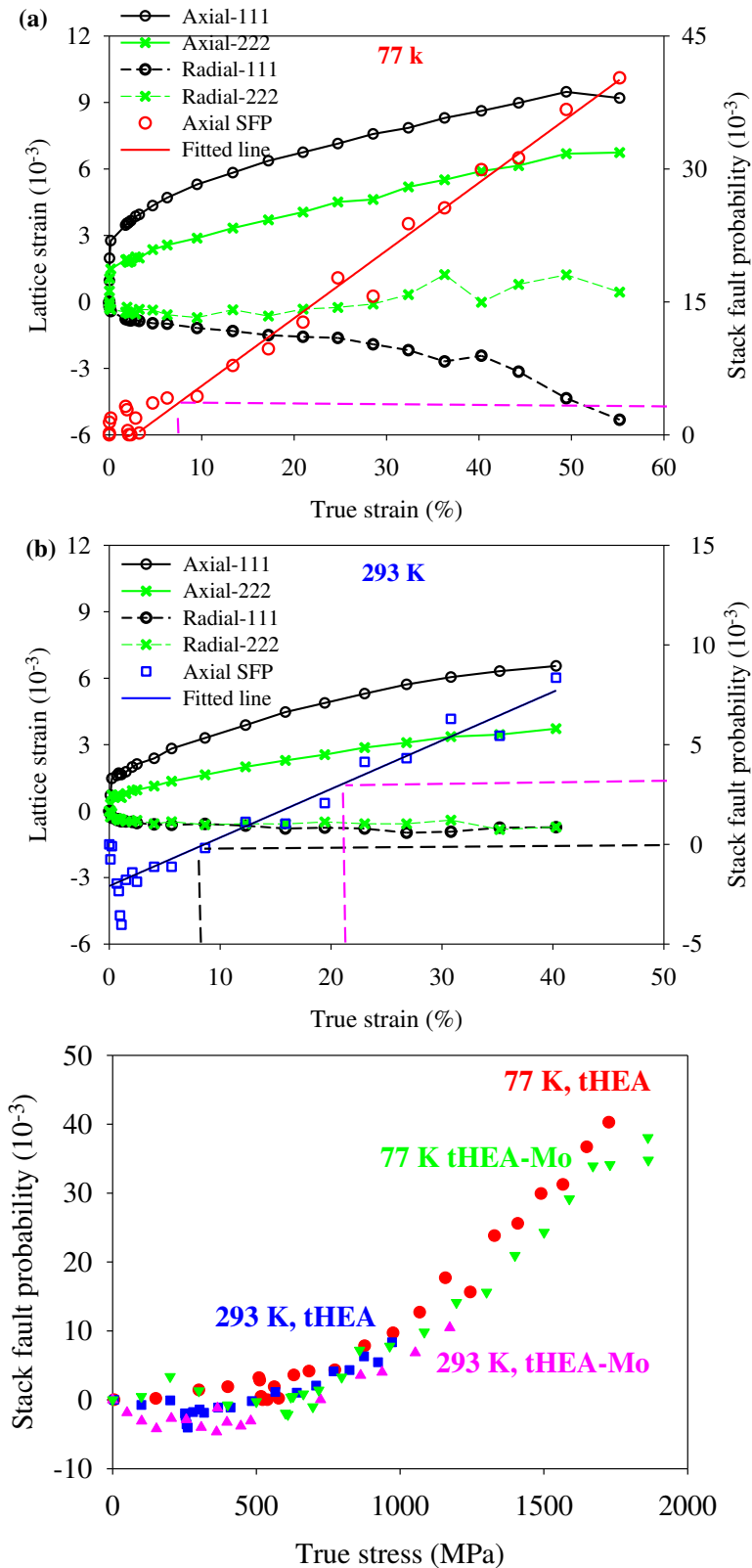


Fig. 4. The (111) first order and (222) second order reflections together with the stacking fault probability as a function of true strain at (a) 77 K and (b) 293 K; (c) stacking fault probability as a function of true stress (tHEA: FeCoCrNi; tHEA-Mo: FeCoCrNiMo<sub>0.23</sub>).

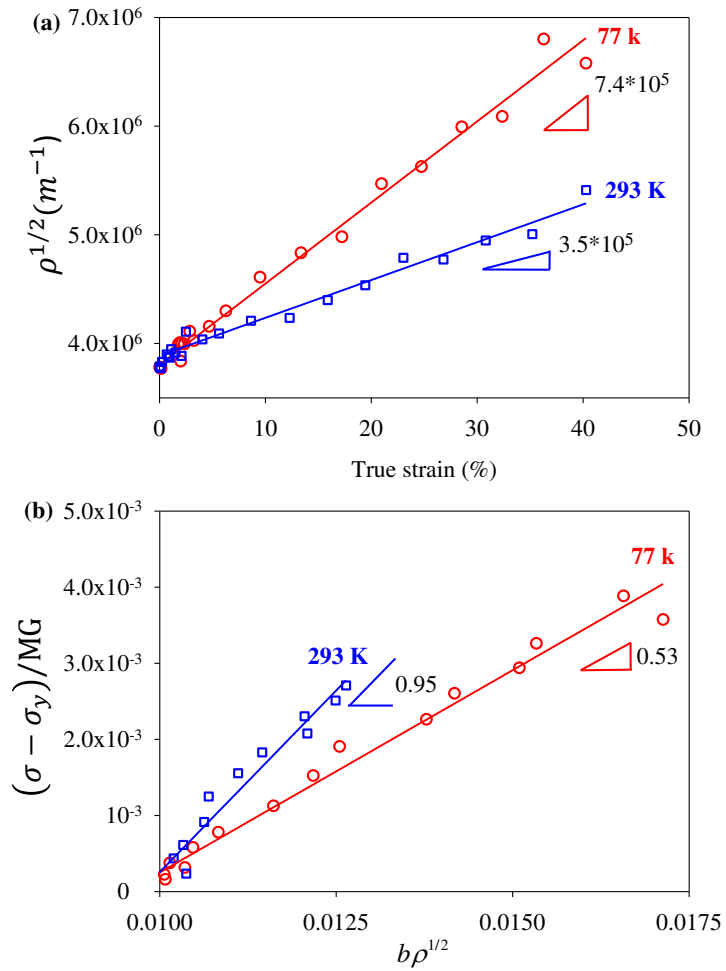


Fig. 5. The evolution of dislocation density versus (a) true strain, and (b) normalised work hardening  $(\sigma - \sigma_y)/MG$  versus  $b\rho^{1/2}$ .

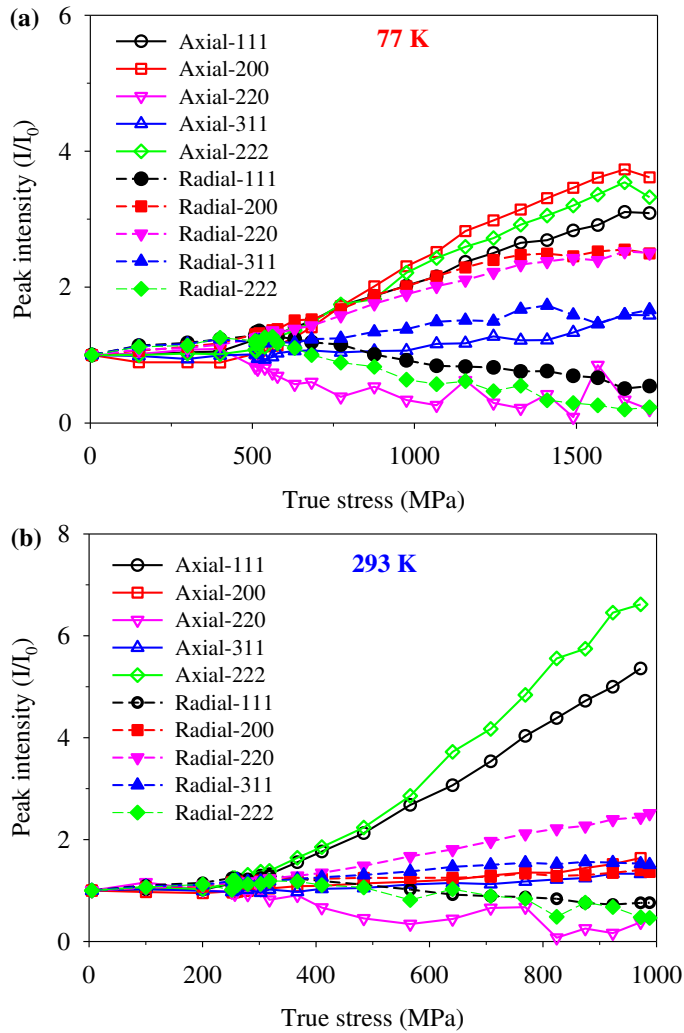


Fig. 6. The evolution of normalized peak intensity along the axial and radial directions in grain families having  $\{111\}$ ,  $\{200\}$ ,  $\{220\}$ ,  $\{311\}$  and  $\{222\}$  crystallographic planes during tensile loading at (a) 77 K, and (b) 293 K.

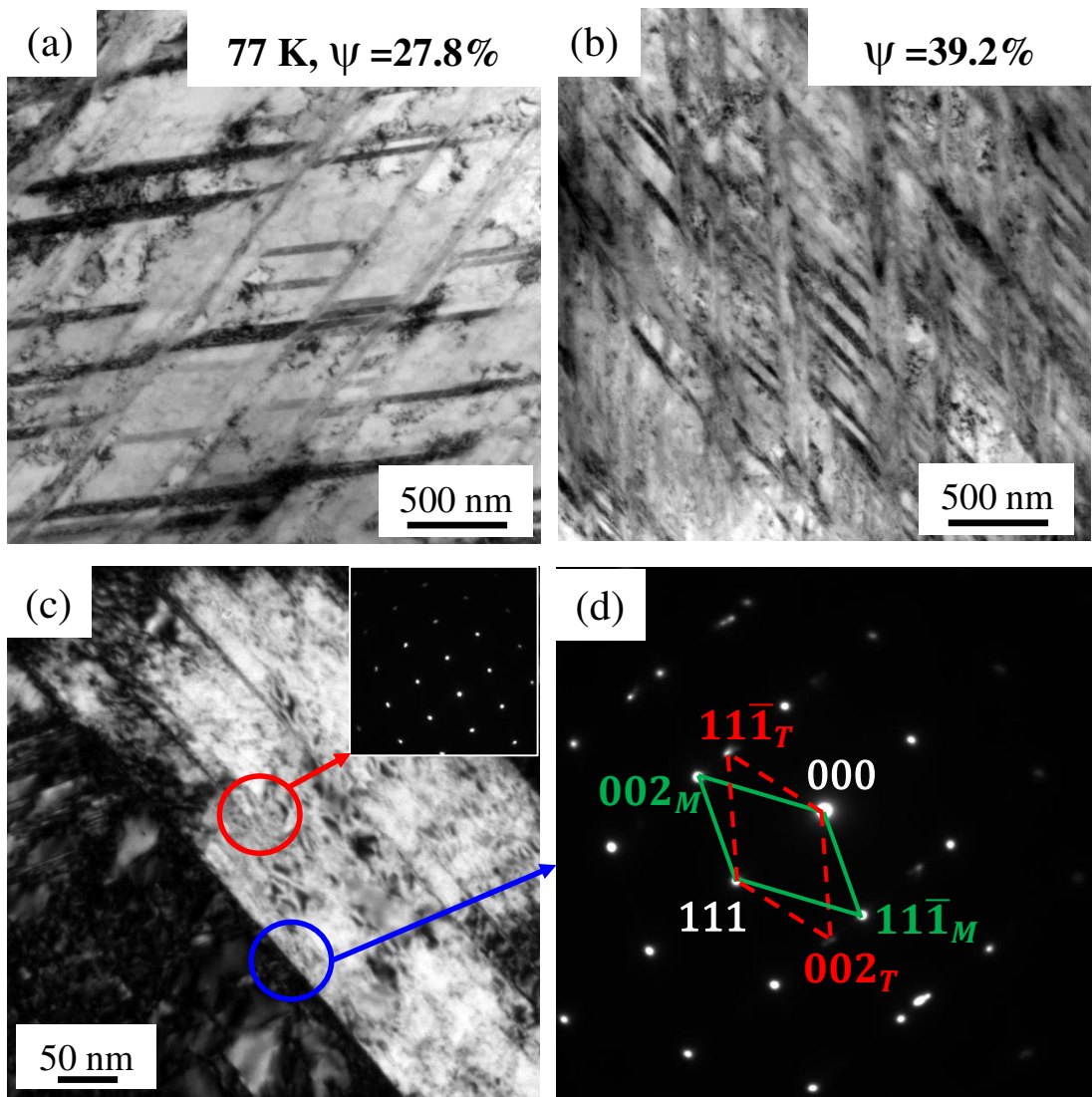


Fig. 7. TEM bright field micrographs of samples with (a) 27.8 % and (b) 39.2% strain at 77 K, which show nano-twins. (c) Higher magnification BF images with an inserted SAD pattern obtained from the matrix and (f) the composite SAD pattern obtained from the blue circled region in Fig. 7c which has contribution from both the matrix and the nano-twin.

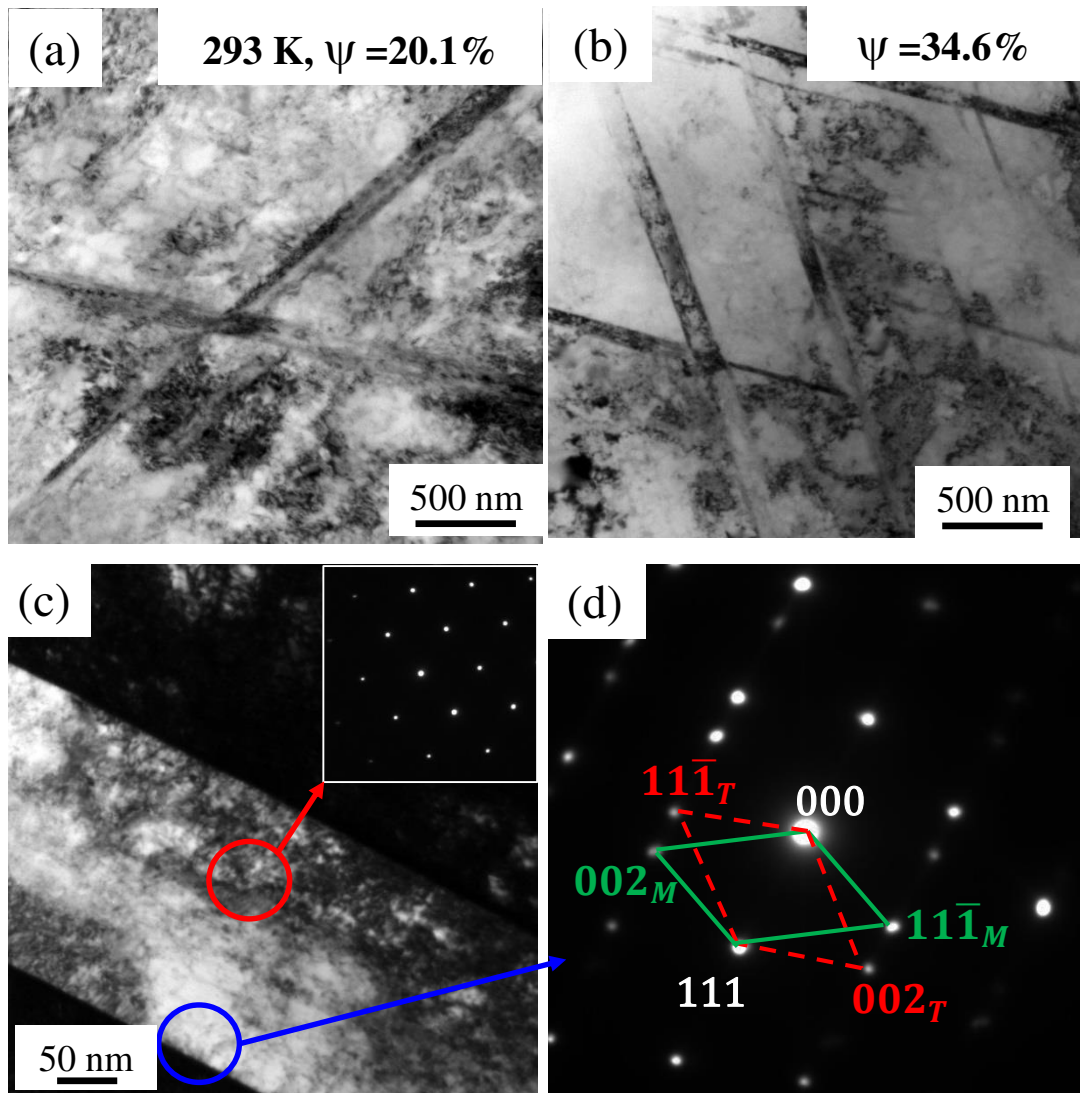


Fig. 8. TEM bright field micrographs of samples with (a) 20.1% and (b) 34.6% strain at 293k, which show nano-twins. (c) Higher magnification BF images with an inserted SAD pattern obtained from the matrix and (f) the composite SAD pattern obtained from the blue circled region in Fig. 8c which has contribution from both the matrix and the nano-twin.